The Astrophysical Journal Letters, 743:L27 (6pp), 2011 December 20 doi:10.1088/2041-8205/743/2/L27

IMAGING SPECTROSCOPY USING AIA DIFFRACTION PATTERNS IN CONJUNCTION WITH *RHESSI* AND EVE OBSERVATIONS

Claire L. Raftery[1], Säm Krucker[2], and Robert P. Lin[3,4]
[1] Space Sciences Lab, UC Berkeley, 7 Gauss Way, Berkeley, CA 94720-7450, USA; claire@ssl.berkeley.edu
[2] Institute of 4D Technologies, School of Engineering, University of Applied Sciences, North Western Switzerland, 5210 Windisch, Switzerland
[3] Physics Department, University of California, Berkeley, CA 94720-7450, USA
[4] School of Space Research, Kyung Hee University, Yongin, Gyeonggi, Republic of Korea
Received 2011 September 9; accepted 2011 November 7; published 2011 November 23

ABSTRACT

Extreme-ultraviolet (EUV) spectroscopy is a very powerful tool that can be used for probing the dynamic response of the solar corona and chromosphere during solar flares. Here we present a unique application of observations from the Atmospheric Imaging Assembly (AIA) on board the Solar Dynamics Observatory using the artifacts of diffraction and dispersion. Using these techniques we can achieve imaging spectroscopy at the resolution of AIA (0.″6 plate scale) and at the revolutionary cadence of the instrument (nominally 12 s) for the brightest (saturated) pixels during solar flares. Analyzing the dispersion and diffraction effects that are observed as a result of the support grids used for the instrument's front filters, we can achieve up to 0.5 Å spectral resolution across the EUV, optically thin passbands. Here we describe the technique used and present the first result of its application—the emission measure distribution for a single pixel at the top of a flaring loop. We analyze the AIA dispersion spectrum in conjunction with Extreme Ultraviolet Variability Experiment observations and spectroscopic and imaging results from the *Reuven Ramaty High Energy Solar Spectroscopic Imager*.

Key words: Sun: corona – Sun: flares – Sun: UV radiation – techniques: imaging spectroscopy – techniques: spectroscopic

Online-only material: color figures

1. INTRODUCTION

Spectroscopic techniques applied to the extreme-ultraviolet (EUV) range of the electromagnetic spectrum can reveal valuable information regarding the dynamics of the solar atmosphere. In the past, many spectroscopic techniques have been employed, from rastering slits to irradiance monitoring. Unfortunately, each technique requires the compromise of either cadence, spatial resolution, or spectral resolution. For example, a slit spectrometer such as the Coronal Diagnostic Spectrometer (Harrison et al. 1995) or the Extreme Ultraviolet Imaging Spectrometer (Culhane et al. 2007) can provide excellent spectral resolution (<1 Å) over a broad spectral range, although the limitations of the slit (or slot) dimensions severely compromise either the field of view or the cadence of any data set.

Instruments such as the Extreme Ultraviolet Variability Experiment on board the *Solar Dynamics Observatory* (*SDO*/EVE; Woods et al. 2010) surmount cadence limitations by measuring the total irradiance of the Sun between 10 Å and 1050 Å with 10 s cadence and 1 Å spectral resolution. The limitation of this technique is the "point source" nature of the observations. Emission is not spatially resolved, but integrated over the entire Sun.

The most popular and user-friendly technique is that of EUV imaging. Here, filters and mirror coatings allow preferential transmission of narrow spectral bands of emission usually ∼10–20 Å wide over large fields of view at high cadences. Over the years, the spatial resolution and cadence of these instruments has vastly improved from 2.″6 pixel^{-1} and 10 minute cadence (e.g., EUV Imaging Telescope; Delaboudinière et al. 1995) to 0.″6 pixel^{-1} and 12 s cadence for the Atmospheric Imaging Assembly (*SDO*/AIA; Lemen et al. 2011). The pitfall of EUV imaging is the width of the passbands. Although they are, in general, on the order of 10 Å wide, many emission lines can form at a wide range of temperatures within that band.

In this Letter, we present a technique that overcomes some of the limitations mentioned above by using the high-cadence, high spatial resolution data of AIA using diffraction artifacts. High-order diffraction patterns also exhibit dispersion effects that can be utilized to obtain pixel-by-pixel spectra from a high-intensity source. In Section 2, we will discuss the AIA instrument and diffraction theory. In Section 3, we discuss our methodology and our preliminary results. These results and future plans are discussed in Section 4.

2. INSTRUMENTATION

The AIA instrument consists of 10 passbands that use a combination of filters and mirror coatings to preferentially transmit emission within a narrow wavelength range (Lemen et al. 2011). These include two thin filters at the entrance aperture of each telescope, each supported by a fine mesh grid (Boerner et al. 2011). Each of the two grids behaves as a set of perpendicular diffraction gratings, generating two orthogonal diffraction patterns per grid, resulting in a total of eight diffraction arms per image. Figure 1 shows an example of this in the 193 Å passband. Following Hecht & Zajac (1974) and Lin et al. (2001), we can fit the intensity at each bright diffraction peak $I(m)$ to identify the original source intensity I_0:

$$I(m) = I_0 \left(\frac{\sin(m\pi b/a)}{m\pi b/a} \right)^2, \quad (1)$$

where m is the order of diffraction, a is the distance from one grid support to the corresponding point on the next, and b is the spacing between grid supports, so $a = b + grid\,width$. Given that there are 70 lines per inch and each support is 29–33 μm

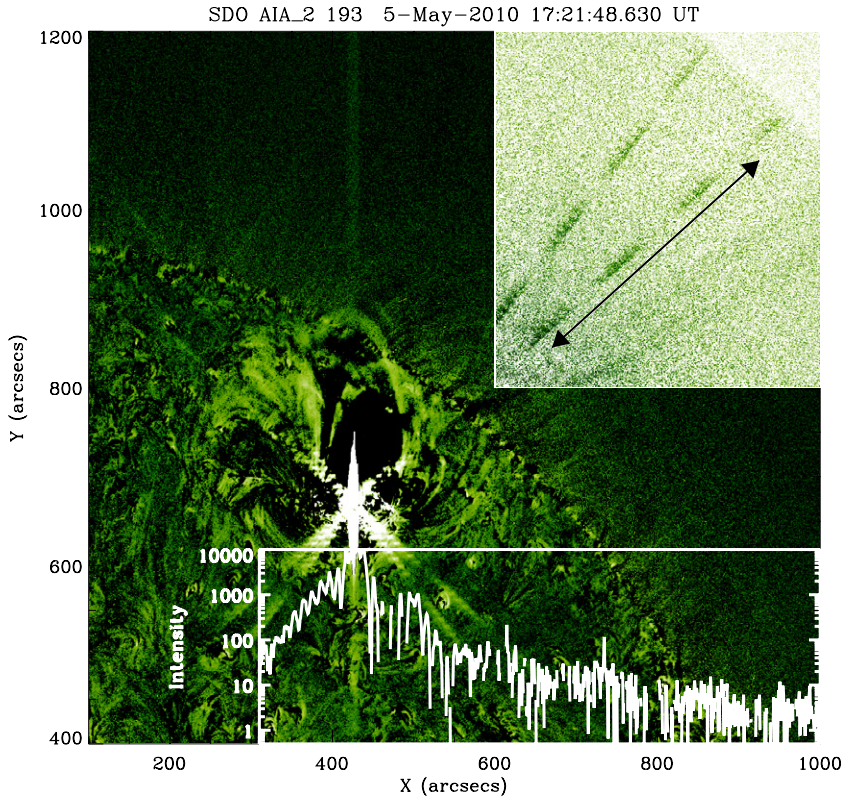

Figure 1. AIA 193 Å difference image (main) with the off-limb diffraction patterns shown in the enhanced box out to 52 orders. The diffraction arm analyzed in this Letter is highlighted by the black arrow and its intensity profile is overplotted in white.

(A color version of this figure is available in the online journal.)

thick, the theoretical value of b/a is 0.91 ± 0.01 (Boerner et al. 2011). This value can also be obtained from fitting Equation (1) to a diffraction intensity profile.

This effect can only be observed when the flux of a given order $I(m)$ is greater than the background flux, placing constraints on the flux of the diffraction pattern's source pixel I_0. Considering average off-limb background values for all of AIA's EUV telescopes, the required source pixel flux is $(10 \pm 8) \times 10^5$ DN pixel^{-1}. Given that saturation level for the AIA EUV telescopes is $\sim 1.6 \times 10^4$ DN pixel^{-1}, diffraction is only observed when pixels are saturated. As such, the true flux of a saturated source cannot be obtained from the image directly, but can be calculated from the diffraction pattern intensity profile following Equation (1) (e.g., Mrozek et al. 2007).

At orders $\gtrsim$12, the effect of dispersion can be observed. This occurs as a result of emission at different wavelengths being diffracted by different angles, much the same as a prism dispersing white light. The angle by which emission is diffracted, θ_m, can be written as:

$$\theta_m = m\frac{\lambda}{a}, \tag{2}$$

where λ is the wavelength and a is the spacing of the mesh grid, as in Equation (1). It is clear that the spatial separation between spectral components $\delta\theta_m$ and therefore the spectral resolution, $\delta\lambda$, will increase with diffraction order. Thus, since AIA's full disk field of view includes up to 60 or more orders, the spectral resolution is significantly improved from that of the *Transition Region and Coronal Explorer* (*TRACE*) with its limited field of view and therefore limited number of orders (Lin et al. 2001; Gburek et al. 2006; Krucker et al. 2011). For example, Figure 1 shows diffraction out to 52 orders while the highest order achieved with *TRACE* was 23 (Lin et al. 2001). Thus, for the 52nd diffraction order in the AIA 193 Å passband, 1 Å spectral resolution corresponds to 3″ (5 pixels) versus only 1.″3 (2 pixels) for *TRACE* at 23 orders.

3. METHOD

Analysis was conducted on one arm of diffraction, highlighted by a black arrow in Figure 1. Background-subtracted images were rotated by $\sim 50^\circ \pm 0.^\circ 2$—the angle by which one front filter grid is rotated relative to the CCD (Lemen et al. 2011). Given that the AIA source pixels are saturated, thermal images from the *Reuven Ramaty High Energy Solar Spectroscopic Imager* (*RHESSI*; Lin et al. 2002) in the 10–17 keV range were used for context imaging (Figure 2). Analyzing *RHESSI* thermal sources in conjunction with pre-flare, non-saturated AIA images (Figure 2, left) enables the identification of various aspects of the flaring loops topology (footpoints, looptop, etc.) that would be otherwise unidentifiable once the AIA images become saturated (Figure 2, right).

Having prepared an image, the diffraction profile can be extracted for every pixel across the width of the diffraction pattern. This is shown schematically in Figure 3 for one looptop pixel. The spatial extent of the diffraction pattern is compared to the *RHESSI* source (top panel, pink contours) and an appropriate pixel is identified. In this case, the selected pixel row is highlighted at high orders (blue inset). The diffraction pattern for that pixel is then extracted (second panel, black dots) and the source flux I_0 is obtained by inverting Equation (1) and fitting it to the intensity profile (red line). It is important to note that all

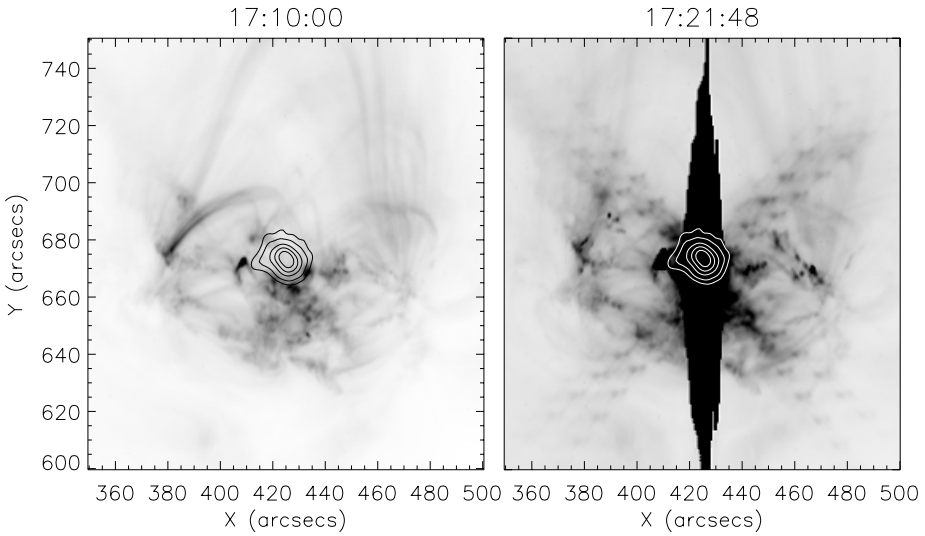

Figure 2. AIA 193 Å pre-flare (left) and saturated (right) images. Overlaid are *RHESSI* 10–17 keV contours imaged at 17:21 UT generated using the CLEAN algorithm and subcollimators 3–9.

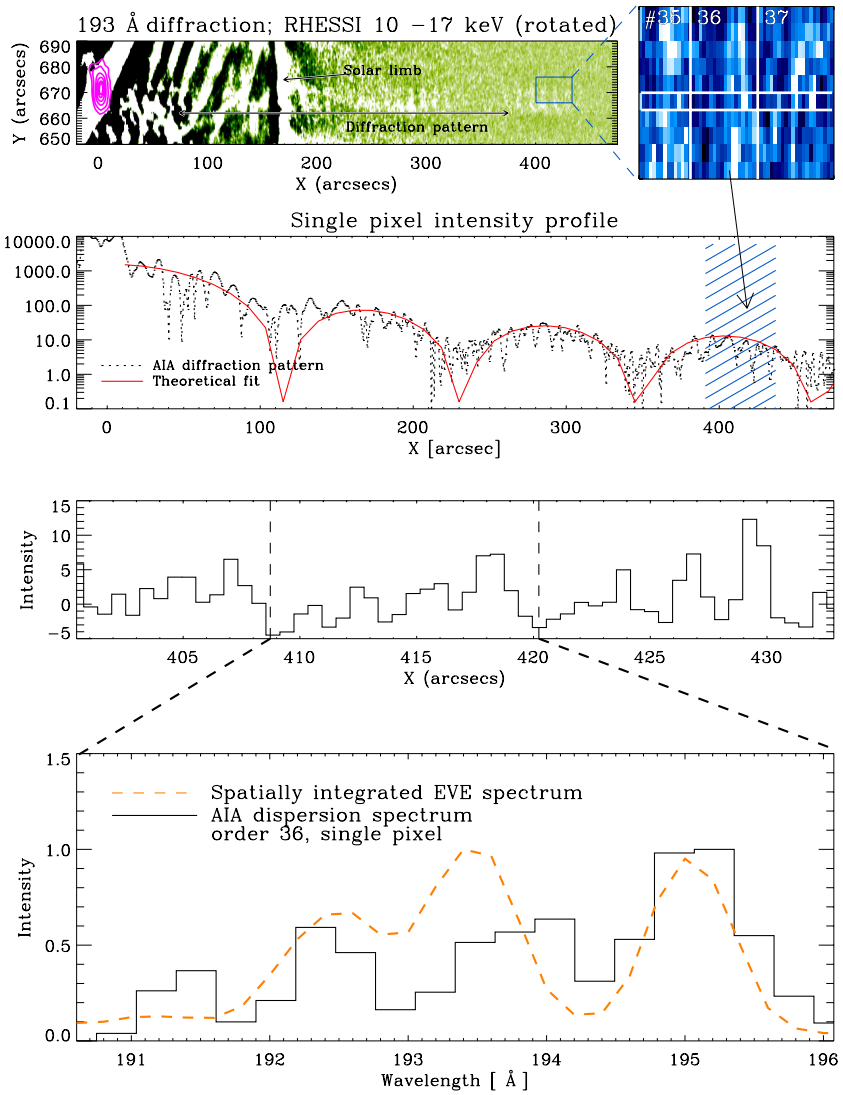

Figure 3. Top left panel: 193 Å rotated difference image (green) overlaid with *RHESSI* 10–17 Å contours (pink). Blue inset shows orders 35–37 of the diffraction pattern, with a single pixel highlighted. Second panel: diffraction profile for selected pixel (black dots) where the *X*-axis represents the distance from the source rather than disk center, with theoretical fit overplotted in red. Third panel shows the intensity of the single pixel profile for orders 35–37. Dashed lines identify order 36 which is converted to a dispersion spectrum in the bottom panel. Overplotted in orange is the spatially integrated EVE spectrum.

(A color version of this figure is available in the online journal.)

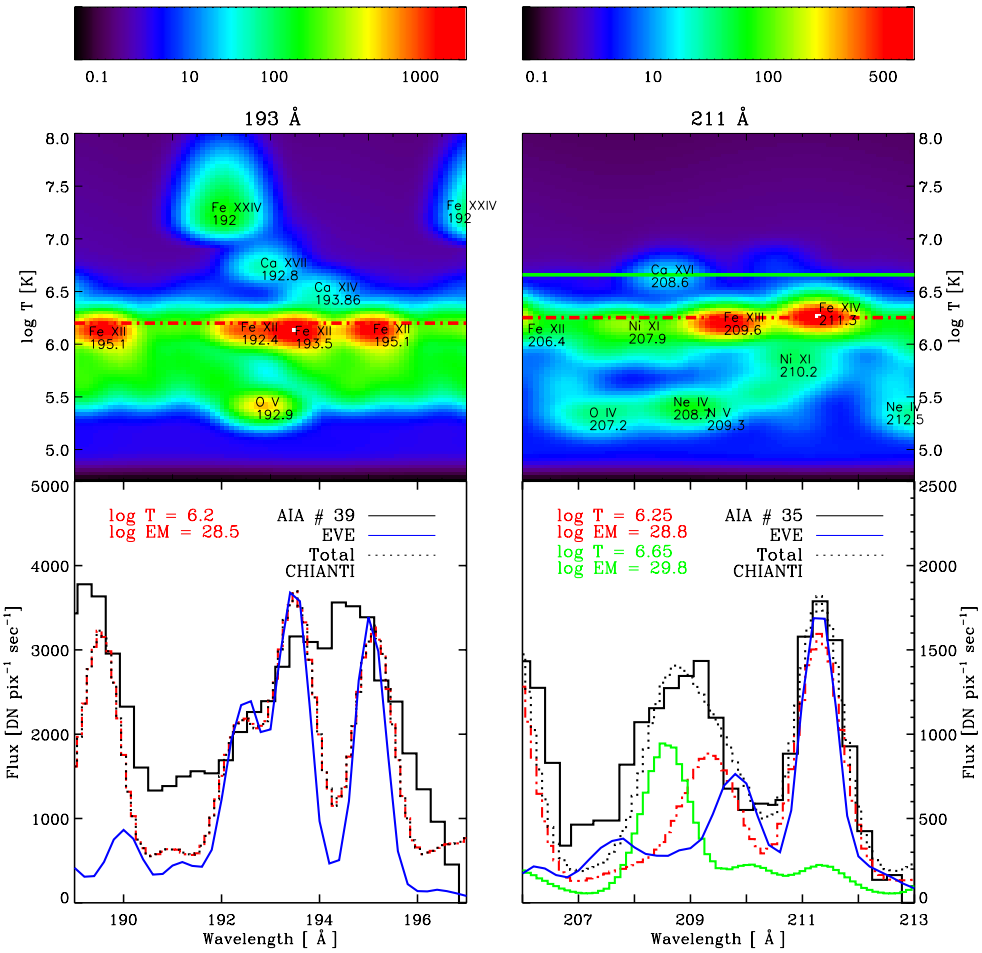

Figure 4. Top plots show stacked synthetic transmitted spectra for 193 (left) and 211 Å (right) passbands. The bottom plots show the observed AIA dispersion spectra (black solid histogram), the corresponding EVE spectra (blue), and the EM-scaled CHIANTI components (green solid and red dot-dashed lines) for different temperature components corresponding to the horizontal dot-dashed lines in the top plots. The black dotted line shows the total contribution for all temperatures.
(A color version of this figure is available in the online journal.)

fitting and individual order analysis was carried out above the solar limb, which is marked on the top panel. The lack of disk emission contamination in the plane of sky orders makes their calibration significantly more reliable.

Following the calculation of I_0, an individual diffraction order is identified. In the third panel of Figure 3, orders 35–37 are identified. These correspond to the orders shown in the blue inset of the top panel and the blue hatch of the second panel. Since the angular distance of each pixel from the source can be measured, converting one order (order 36, between dashed lines) to wavelength, i.e., a dispersion spectrum, can be achieved following Equation (2). The result is shown in black in the bottom panel of Figure 3. To ensure the dispersion was accurately converted (individual pixel uncertainties can result in up to 0.5 Å wavelength discrepancies), the dispersion spectra were compared to co-temporal, spatially integrated, background-subtracted spectra from EVE (Figure 3 bottom panel, orange dashed line). Given the discrepancies in field of view (a single AIA pixel versus full disk with EVE), and the fact that we are not using the absolute flux of the EVE observation, we arbitrarily scale EVE data to match the intensity of AIA for alignment purposes only. This proved to be a useful step, in particular for discriminating between multiple lines in particularly noisy AIA spectra. Finally, the AIA dispersion spectrum is scaled so that the integrated spectrum flux equals the original source flux I_0 as all emission observed at the zeroth order must match the integrated flux observed at each subsequent order.

To fit the dispersion spectrum, a series of isothermal CHIANTI spectra (Dere et al. 1997, 2009) were generated with a fixed emission measure (EM) of 10^{28} cm^{-5} in units of photons cm^{-2} sr^{-1} s^{-1} Å^{-1} and convolved with the wavelength response function of the corresponding AIA telescope. Each spectrum, now in units of DN pixel^{-1} s^{-1} Å^{-1}, is convolved with a pseudo-point-spread function in the wavelength direction that is calculated based on the spectral resolution of the passband and the diffraction order using Equation (2). The spectral resolution used here varies between ∼0.3 and 0.7 Å depending on the wavelength and order number. For ease of analysis, these spectra were stacked in order of temperature to produce a "spectrogram" of wavelength versus temperature. Two examples of this are shown in Figure 4 (top left and right for 193 and 211 Å, respectively). Color corresponds to flux in units of DN pixel^{-1} s^{-1} Å^{-1} and the X- and Y-axes are the wavelength and log temperature, respectively. The final stage in preparing the synthetic spectra was to account for contamination from neighboring diffraction orders. Rather than attempt to deconvolve overlapping lines from adjacent orders in the dispersion

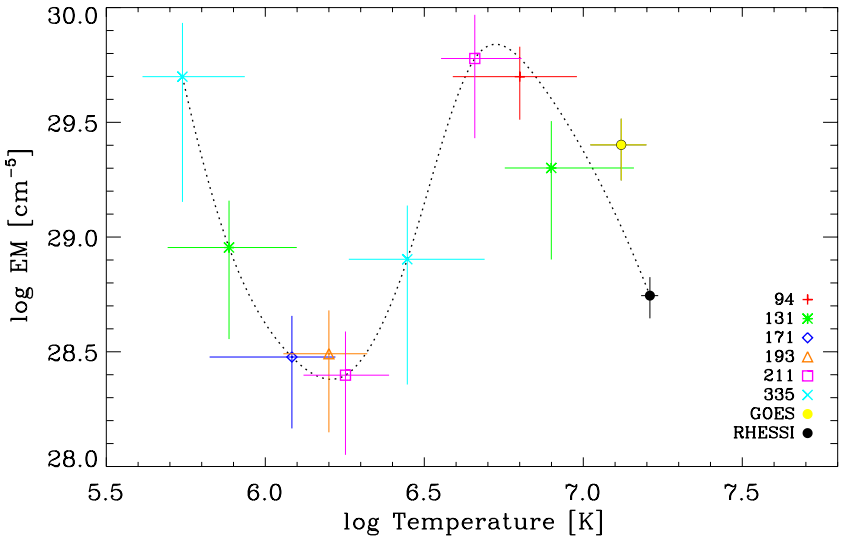

Figure 5. Results from fitting each AIA dispersion pattern for a single co-aligned pixel at a single time with isothermal CHIANTI spectra. *RHESSI* and *GOES* spectroscopic results are also shown.

(A color version of this figure is available in the online journal.)

spectrum, they were added into the synthetic spectra by calculating the overlap using Equation (2). An example of this can be seen in the top left of Figure 4. Here we see two features formed at log $T \sim 7.2$. In fact, this is the single Fe XXIV line feature formed at 192 Å from order 36 (at 192 Å) and again from order 37 (at 197 Å). This is also observed for Fe XII 195 Å line which is seen at 195 Å for order 36 and 189 Å for order 35. This is why there is a distinct lack of emission in EVE at 189 Å (blue line, bottom plot): what is observed in AIA is not a real line formed at 189 Å but rather it is the 195 Å line from order 35 that is impinging on the 36th order.

Once the synthetic spectrograms were generated, features corresponding to those observed in the AIA dispersion spectrum were identified by eye. For example, the 193 Å example in Figure 4 (left column) shows four peaks in the AIA dispersion spectrum (black histogram, bottom left panel). The relative intensities of these line features can all be accounted for by one isothermal spectral component corresponding to the red horizontal dot-dashed line in the top left plot. It is possible to isolate this temperature (or range of temperatures as indicated by error bars in Figure 5) because the isothermal spectra at other temperatures either contain peaks at other wavelengths or are lacking the lines required to reproduce this fit.

In the case where no single temperature satisfied all peaks in the dispersion spectrum, multiple temperatures were used. An example of this is shown in the right column of Figure 4 for the 211 Å passband. Here, the CHIANTI spectrum at log $T =$ 6.25 K (red dash-dotted line in upper and lower right panels) matches well with the primary peak at 211.5 Å and partially so for the secondary peak at 208 Å. However, it is clear that it is not sufficient to model the secondary AIA peak completely both due to insufficient relative flux, and an offset between the peak wavelength of the secondary dispersion pattern peak (209 Å) and the smaller peak in the log $T = 6.25$ K spectrum (209.5 Å). Therefore, we include a second CHIANTI component at log $T = 6.65$ K (green solid line). The combined fluxes of these two isothermal spectra (bottom right panel, dotted black line) produce a more accurate model of the AIA dispersion spectrum. In all passbands, the primary source of uncertainty in temperature comes from the broad temperature range over which an individual line is formed. This can be limited by disregarding temperatures at which there are other prominent lines that are not observed in the dispersion spectrum. The uncertainty in temperature varies from 0.1 to 3 MK depending on the passband.

In addition to identifying the temperature of the spectral components, their intensity can be adjusted to match that of the dispersion spectrum. Following the Coronal Approximation (Mariska 1993), the flux of an emission line is proportional to the EM. As such, scaling the intensity of the CHIANTI components to match that of the calibrated dispersion pattern is a direct representation of the EM. There are many sources of uncertainty, such as the angle of rotation relative to the CCD, identification of the saturated source pixel, and poor signal to noise at high orders. However, the primary source of uncertainty in the calculation of the EM is the calculation of I_0 for each pixel, given that the dispersion spectra are normalized to this value. This has been reduced by fitting I_0 using only accurately background-subtracted, off-disk orders of diffraction and is conservatively estimated to be correct to ~40%. The final source of uncertainty is in the reliability of CHIANTI in the 94 and 131 Å passband (P. Boerner 2011, private communication). However, it is believed that since this analysis is close to the peak of the flare and the higher-temperature CHIANTI calculations are believed to be more reliable, the majority of the emission in this passband will be from the better understood hot component and so the CHIANTI calculations can be assumed to be correct. In fact, when a line is present in the dispersion spectrum that is not observed in CHIANTI, a more detailed analysis using forward modeling techniques may even help to identify lines in need of further atomic processing, thus improving the AIA temperature response functions.

Combining these results from the same saturated source pixel in all optically thin EUV telescopes results in the EM curve shown in Figure 5. This analysis is completed through the inclusion of the spectral results from *RHESSI* and *GOES*. The *RHESSI* spectrum was analyzed for 12 s centered around the time of the AIA image (17:21:48 UT). The spectrum was fit using an isothermal Bremsstrahlung component only (Holman et al. 2003) as at this time in the flare (~4 minutes after the hard X-ray peak and 3.5 minutes after the soft X-ray peak) there is

little or no evidence for non-thermal emission. Additionally, the filter ratios of the *GOES* channels were utilized to obtain the temperature and EM at the time of the AIA image following White et al. (2005). Given that we are analyzing the results of a single AIA pixel of dimensions $0\farcs6 \times 0\farcs6$, the total temperature and EM values from *RHESSI* and *GOES* were normalized by the area of the source as observed with *RHESSI*. This may lead to some uncertainty as we are assuming that the emission is distributed uniformly throughout the entire source which of course will not be the case. However, as the top panel of Figure 3 shows, the pixel in which we are interested falls close to the center of the *RHESSI* source so this assumption is not entirely unwarranted. Similarly, assuming that the *GOES* plasma originates from the same source as that observed by *RHESSI* may lead to discrepancies. Again, the thermal nature of the *RHESSI* source, and the fact that we are observing the loop apex, justifies this assumption.

4. RESULTS AND CONCLUSIONS

Figure 5 shows the first results of the dispersion spectroscopy technique as applied to AIA for a single pixel close to the apex of a flaring loop three minutes after the peak of an M-class flare. This EM distribution curve has been obtained through fitting one or more isothermal CHIANTI spectra to dispersion spectra observed in six AIA passbands and combining them with the spectral results from *RHESSI* and *GOES*. Given that this analysis was applied to the early decay phase of the flare, it is expected that not only should we see the hot, flaring material but also plasma that has begun to cool. Figure 5 shows that this is indeed the case. We can observe the remnants of the very hot material with the X-ray instruments at $>10^7$ K along with increased emission levels between 4 and 6 MK ($\log\ T = 6.6$–6.8). We can see a significant deficit of material at 1 MK ($\log\ T = 6$) where the nominal coronal material has been heated to much higher temperatures during the flare. Finally, there is still a large volume of material along the line of sight at cooler ($<10^6$ K) temperatures. This may be as a result of plasma that was heated early on, now cooling within the flare loop, or due to chromospheric plasma brightening due to, e.g., compression during the evaporative phase of the flare (e.g., Raftery et al. 2009; Milligan et al. 2006; Brosius 2009). While these results are typical, the strength of this analysis is understanding that this technique can be expanded to generate a differential emission measure curve for every saturated AIA pixel within the flare for each image during the event. Under the right conditions, we will be able to analyze the dynamics of flaring plasma in time, space, and temperature.

The limitations of this analysis come from the requirement for saturation, hence flare emissions are most suitable. Events that occur close to the limb are ideal for this analysis as it allows us to observe diffraction patterns on the plane of the sky where they are not contaminated by disk emissions. Of course, the dependence of intensity on order number suggests that as we go to higher orders (i.e., beyond the limb), the intensity will drop. On the other hand, the higher the order, the better the spectral resolution. Thus, there is a fine balance to be achieved in selecting the most appropriate order. Therefore, simple, compact flares with small ($\lesssim 10''$) footpoint area or narrow, well-defined flare ribbons with uncontaminated diffraction profiles are ideal candidates, in particular if they are located within $\sim 100''$ of the solar limb. Instrumentally, observations must have exposure times long enough to allow saturation to occur. Ideally, longer exposures interspersed with shorter, unsaturated images are optimal.

Despite the restrictions on this analysis, it is an extremely powerful technique that will enable innovative analysis techniques that cannot be achieved by any other means, including restoration of saturated AIA pixels and EUV imaging spectroscopy at the resolution and cadence of AIA. Here we can expand the already impressive data set provided by AIA to include spatially resolved spectral analysis of the distribution of plasma throughout a flaring loop and the timescales over which these distributions change without, e.g., the timing restrictions of rastering spectroscopy or the limiting spatial resolution of irradiance monitoring.

This research is supported in part by NASA contract NAS5-98033. R. P. Lin was supported in part by WCU grant No. R31-10016 funded by the Korean Ministry of Education, Sciences, and Technology.

REFERENCES

Boerner, P., Edwards, C., Lemen, J., et al. 2011, Sol. Phys., in press
Brosius, J. W. 2009, ApJ, 701, 1209
Culhane, J. L., Harra, L. K., James, A. M., et al. 2007, Sol. Phys., 243, 19
Delaboudinière, J.-P., Artzner, G. E., Brunaud, J., et al. 1995, Sol. Phys., 162, 291
Dere, K. P., Landi, E., Mason, H. E., Monsignori Fossi, B. C., & Young, P. R. 1997, A&AS, 125, 149
Dere, K. P., Landi, E., Young, P. R., et al. 2009, A&A, 498, 915
Gburek, S., Sylwester, J., & Martens, P. 2006, Sol. Phys., 239, 531
Harrison, R. A., Sawyer, E. C., Carter, M. K., et al. 1995, Sol. Phys., 162, 233
Hecht, E., & Zajac, A. 1974, Optics (Addison-Wesley Series in Physics; Reading, MA: Addison-Wesley)
Holman, G. D., Sui, L., Schwartz, R. A., & Emslie, A. G. 2003, ApJ, 595, L97
Krucker, S., Raftery, C. L., & Hudson, H. S. 2011, ApJ, 734, 34
Lemen, J. R., Title, A., Akin, D., et al. 2011, Sol. Phys.
Lin, A. C., Nightingale, R. W., & Tarbell, T. D. 2001, Sol. Phys., 198, 385
Lin, R. P., Dennis, B. R., Hurford, G. J., et al. 2002, Sol. Phys., 210, 3
Mariska, J. T. 1993, The Solar Transition Region (Cambridge: Cambridge Univ. Press)
Milligan, R. O., Gallagher, P. T., Mathioudakis, M., et al. 2006, ApJ, 638, L117
Mrozek, T., Tomczak, M., & Gburek, S. 2007, A&A, 472, 945
Raftery, C. L., Gallagher, P. T., Milligan, R. O., & Klimchuk, J. A. 2009, A&A, 494, 1127
White, S. M., Thomas, R. J., & Schwartz, R. A. 2005, Sol. Phys., 227, 231
Woods, T. N., Eparvier, F., Hock, R., et al. 2010, Sol. Phys., in press